Proceedings of IDETC/CIE 2006
ASME 2006 International Design Engineering Technical Conferences &
Computers and Information in Engineering Conference
September 10-13, 2006, Philadelphia, Pennsylvania, USA

DETC2006-99417

OPTIMAL DESIGN WITH NON-NORMALLY DISTRIBUTED RANDOM PARAMETERS, CONDITIONAL PROBABILITY, AND JOINT CONSTRAINT RELIABILITIES: A CASE STUDY IN VEHICLE EMISSIONS REGULATIONS TO ACHIEVE AMBIENT AIR QUALITY STANDARDS

Kuei-Yuan Chan , Steven J. Skerlos , Panos Y. Papalambros *

{chanky,skerlos,pyp}@umich.edu

Department of Mechanical Engineering

University of Michigan

Ann Arbor, Michigan, 48109

ABSTRACT

Making appropriate environmental policy decisions requires considering various sources of uncertainty. An air pollution example is formulated as a design optimization problem with probabilistic constraints, also referred to as reliability-based design optimization (RBDO). Environmental applications with a large number of constraints and significant model complexity present special challenges. In this paper an efficient active set strategy is integrated with a reliability contour surface approach to solve probabilistic problems with non-normal variable probability distributions. Discrete random parameters, which result in Bayesian probability, are also present and they are incorporated using delta function approximations. Joint constraint reliability that considers satisfying all regulatory constraints is also discussed. A demonstration example of setting the optimal vehicle speed limit while maintaining high reliability for CO and NOx standards of a residential area near two highway systems is included.

*Corresponding author, Phone/Fax: (734) 647-8401/8403

1 Introduction

Design for the environment aims to achieve design performance with minimal environmental, health, and safety impact over the product life cycle. Such design decisions are subject to large sources of uncertainty. Uncertainty in environmental vehicle design arises from life cycle emissions variables and from ambient parameters that dictate pollutant concentrations in the environment and are outside the influence of the designer. In Fig.1 we illustrate a specific situation of an airshed within which a population is subject to vehicle pollutants generated by two nearby roads. We assume that the airshed is subject to frequent violations of the National Ambient Air Quality Standards (NAAQS) for both Carbon Monoxide (CO) and Nitrogen Oxides (NOx) and that these two roads are the exclusive sources of the emissions. We further assume that we are interested in regulating CO and NOx from these roads such that the NAAQS concentrations for these pollutants are met with a known reliability (e.g., 90%). It is evident that the actual pollution concentrations in the airshed depend on numerous factors, such as the combustion and emissions control systems of the vehicles on the road, driver responses to posted speed limits, traffic density, location of roads and receptors, wind speed and direction, and atmospheric mixing conditions that depend on temperature and season. In

this system, only the vehicle design, combustion conditions, and emissions control systems of individual vehicles are under the direct influence of product designers.

The policymaker, whose role is to simultaneously promote human health and economic development, must consider how the uncertainty arising from vehicle emissions comes together with the uncertainty from the ambient environment to impact individuals living in the airshed. The policymaker has numerous regulatory options to bring the airshed into compliance with the NAAQS, including fuel economy standards and incentives [1, 2], pollutant emissions standards [3], progressive taxation on polluting vehicles [4], reducing traffic density using tolls [5, 6], and modifying vehicle speed limits [7]. Regardless of the policy mechanism, the goal is to achieve stricter environmental targets with a given reliability while minimizing impact on the economy, consumer choice, safety, and transportation time.

The policy design problem described above can be considered within the class of Reliability-Based Design Optimization (RBDO) problems described in the literature [8, 9], even though this problem has a number of features which distinguish it from problems previously investigated. Specifically, RBDO research to date has primarily focused on engineering design variables that are continuous, time-invariant, and with symmetric distributions. Extensions to problems with ecosystem variables requires consideration of random parameters that are non-gaussian [10], skewed [11], time and season dependent [12], and sometimes discrete [13]. This paper considers these extensions in the context of Fig.1. It also considers an issue that has received little attention in the literature: namely the joint reliability of constraint satisfaction. This issue is critical in environmental policymaking as the goal is not to independently establish a 90% reliability of complying with the CO standard and a 90% reliability for complying with the NOx standard, but rather to establish a 90% probability of not violating *either* standard. In other words, the number describes the probability that any constraint is violated. This issue increases in importance as the number of receptors and pollutants to be regulated increases, to the extent that this increases the likelihood of a higher number of active constraints at the optimum.

In contrast to RBDO approaches, previous research considering uncertainty in the impact of engineering design decisions on environmental quality has focused on the use of simulation techniques and/or sensitivity analysis (e.g., see [14–16]). These techniques typically utilize models of remote sensing data from environmental parameter observations created by either Taylor series expansions or sampling techniques such as Monte Carlo Simulation (e.g., [17–22]). However, these models are not applicable to analytical formulations, such as RBDO, that would hold several advantages for the problem posed in Fig.1. For instance, one can consider the airshed problem as a basic building block that could be extended to analyze an entire city. As additional roads, road segments [23], and receptors are applied to

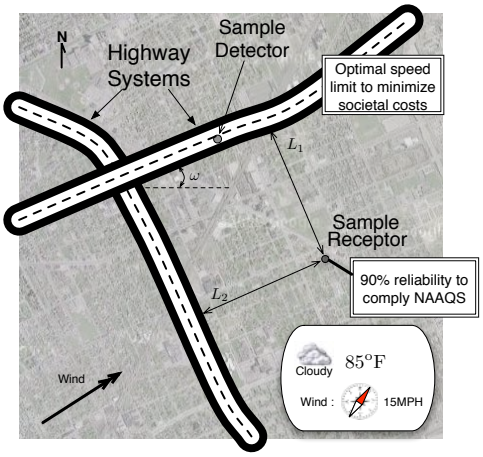

Figure 1. Optimal speed limit considering the compliance of the receptor air quality under wind, traffic, ambient conditions uncertainties

the basic formulation, the use of sampling techniques to evaluate probabilistic constraints would require too many computations for practical application. Even if the computations could be completed in a reasonable amount of time, finding a means to integrate the sampling techniques into an optimization algorithm would pose significant challenge and greatly increase computation. A simulation-based approach would also be less amenable to post-optimality analysis of the solution produced.

Here we propose to investigate environmental quality problems from a policy perspective as RBDO formulations, by extending the method developed in [24] and [25]. With respect to modeling uncertain environmental parameters using analytical probability distributions, a significant amount of research has been performed. For instance, Dabberdt et al. [26] used probabilistic uncertainty to access the impact levels of a 3-hour H_2SO_4 release accident on a neighborhood. Zhang et al. [11] calculated the skewness and kurtosis of on-road CO and HC emissions and concluded that these emissions can be modelled well as Γ-distributions. Despite these efforts, very little effort has been made so far to utilize these models within a policy design optimization framework. The closest research is that of Liu et al. [27], which used a linear chance-constrained programming method to study the impact of regional air quality under uncertainty. Although this method considers both fuzzy and random variables/parameters in an optimization framework, linear chance-constrained formulation has only limited application to environmental problems, which tend to be highly nonlinear.

Eq.(1) is a generalized single-objective RBDO formulation that can be applied to the airshed problem with random design variables $\mathbf{X}$, random parameters $\mathbf{P}$, deterministic design variables $\mathbf{x}$ and deterministic parameters $\mathbf{p}$. The objective f is a function of deterministic quantities, namely the mean values of all random

quantities in the formulation and $\mathcal{K}$ is the constraint set.

$$\min_{\boldsymbol{\mu}_\mathbf{X},\mathbf{x}} f(\boldsymbol{\mu}_\mathbf{X},\boldsymbol{\mu}_\mathbf{P},\mathbf{x},\mathbf{p})$$
$$\Pr[g_j(\mathbf{X},\mathbf{P},\mathbf{x},\mathbf{p})>0] \le P_{\mathrm{f},j}\ \forall j \in \mathcal{K} \quad (1)$$

Constraints with random variables are formulated so that the probability of constraint violation is less than or equal to an acceptable failure limit $P_{\mathrm{f},j}$. Deterministic constraints (i.e., constraints that are not functions of any random quantities) are considered in the probabilistic form as a special case with the failure probabilities $P_{\mathrm{f},j}$ being zero. Equality constraints are not explicitly included in this formulation.

Applying existing RBDO solution methods to Eq.(1) is not possible due to the existence of discrete random parameters (e.g., atmospheric mixing conditions). In addition, existing solution methods for handling non-normal variables would slow the solution process, such that adding additional constraints (as required to model large urban areas) would not be practical (e.g., see [28–30]). A further development required is the consideration of joint constraint violation probabilities. At the solution point to Eq.(1), the probability of violating any given constraint is determined by $P_{\mathrm{f},j}$. Alternatively, a joint constraint reliability formulation is provided in Eq.(2).This type of constraints are often referred to system reliability in the literature. Mathematically system reliability and joint reliability are the same, however, in practice system reliability related to the overall reliability of mixed parallel and series systems. Joint reliability on the other hand is a statistical term which used to represent general concept as in Eq.(2)

$$\min_{\boldsymbol{\mu}_\mathbf{X},\mathbf{x}} f(\boldsymbol{\mu}_\mathbf{X},\boldsymbol{\mu}_\mathbf{P},\mathbf{x},\mathbf{p})$$
$$\Pr\left[\bigcup_j g_j(\mathbf{X},\mathbf{P},\mathbf{x},\mathbf{p})>0\right] \le P_\mathrm{f}\ \forall j \in \mathcal{K} \quad (2)$$

This paper solves the problem of Eq.(2) in a computationally efficient manner as would be needed to scale the problem to large urban systems. Section 2 discusses methods for handling non-normal random variables/parameters, discrete random probabilities, and joint constraint reliability within the active set strategy for design optimization detailed in [25]. The application of these methods to the problem at hand is described in Section 3 with results and discussion provided in Section 4.

2 Methodology

2.1 Optimization Algorithm

A sequential linear programming (SLP) algorithm with active set strategy is used as developed in [24, 25]. In this algorithm, constraint activities at each design iteration are identified. Only the probabilities of the set of active and potentially active constraints (the working set) is calculated with high accuracy.

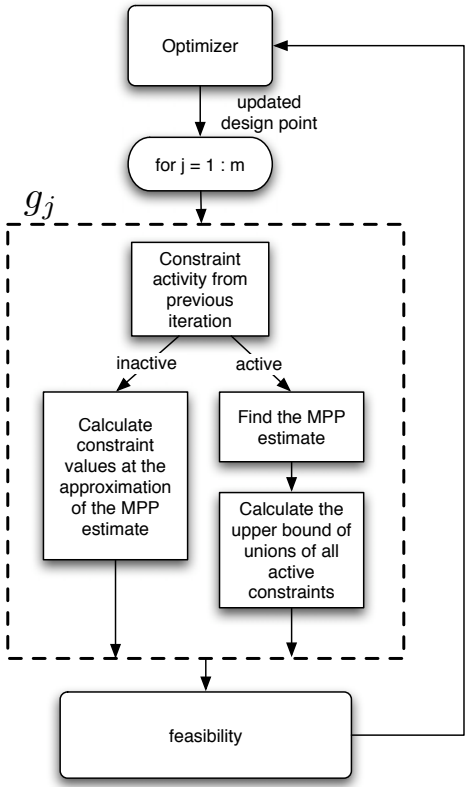

Figure 2. Algorithm Concept

Approximations of failure probability with lower accuracy (and hence computational cost) are satisfactory for constraints that are not in the working set. A flowchart for the method is given in Figure 2.

Feasibility of design $\boldsymbol{\mu}_\mathbf{X}^k$ considers all m constraints. Once all constraint activities are identified, the upper bound of the joint constraint reliability is calculated. This upper bound is used as the feasibility of the current design point and the information is sent back to the optimizer where the working set is updated. The optimizer generates a new design point and working set, until convergence.

2.2 Random and Discrete Parameter Uncertainty

During optimization, values of design variables change with each iteration while parameters remain fixed. Eq.(3) shows a constraint g of random design variables $\mathbf{X}$ and random design parameters $\mathbf{P}$.

$$\Pr[g(\mathbf{X},\mathbf{P})>0] = \int_{g(\mathbf{X},\mathbf{P})>0} \cdots \int f_{\mathbf{XP}}(\mathbf{x},\mathbf{p}) d\mathbf{x} d\mathbf{p} \quad (3)$$

Since at a given design point the nominal values of $\mathbf{X}$ (i.e., $\boldsymbol{\mu}_\mathbf{X}$) are fixed, one can treat a random design parameter as a ran-

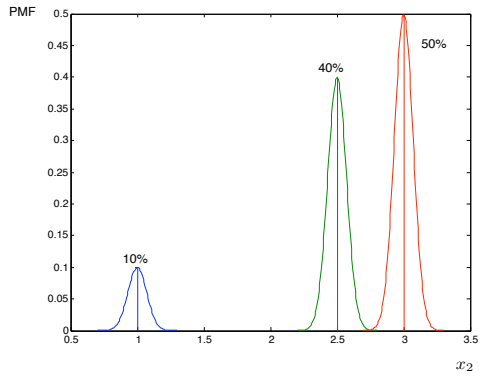

Figure 3. Probability Mass Function of X_2 and Its Approximations

dom design variable with a fixed nominal value. When treating parameters as design variables a new design vector $\mathbf{X}' = [\mathbf{X}, \mathbf{P}]$ is created. Given the ability to treat parameters as "unchanging variables" in an optimization routine, random parameters $\mathbf{P}$ will be included within $\mathbf{X}$ in the rest of this paper for notational simplicity.

Consider the example of $g(\mathbf{X}) = X_1 + X_2$. Let X_1 have a standard normal distribution and let X_2 have the following discrete distribution:

$$X_2 = \begin{cases} 1, & 10\% \\ 2.5, & 40\% \\ 3, & 50\% \end{cases} \tag{4}$$

The probability of constraint violation is calculated using total reliability theory as:

$$\begin{aligned} \Pr[g(\mathbf{X}) > 0] &= \Pr[g(\mathbf{X}) > 0 | x_2 = 1] \times 10\% \\ &+ \Pr[g(\mathbf{X}) > 0 | x_2 = 2.5] \times 40\% \\ &+ \Pr[g(\mathbf{X}) > 0 | x_2 = 3] \times 50\% \end{aligned} \tag{5}$$

To represent X_2 in a continuous optimization algorithm, a scaled Gaussian distribution, which works as a delta function approximation, is used to approximate each function value in the probability mass function (PMF) plot.

The PMF of X_2 can then be approximated as a continuous PDF via Eq.(6) where ϕ is the normal PDF.

$$f_{X_2} \approx \phi(1,\sigma) \times 10\% + \phi(2.5,\sigma) \times 40\% + \phi(3,\sigma) \times 50\% \tag{6}$$

The accuracy of this approximation depends on the value of σ. The smaller σ is, the better approximation it becomes.

2.3 Non-Gaussian Uncertainty

The calculation of probabilistic constraints in Eq.(1) represents the majority of function evaluations during optimization. Several methods have been proposed to improve the efficiency and accuracy of calculating constraint probabilities [31]. Importantly, each of these methods has essentially focused on Gaussian distributed variables. The presence of non-Gaussian distributions makes calculating constraint Eq.(3) more challenging. Methods for dealing with non-gaussian distributed random quantities have been discussed in the literature [28, 30, 32], but they are computationally expensive and not well-suited for large problems, such as the present air quality policy-setting problem.

Significant advantages in computing probabilities follow from the rotational symmetry of a Gaussian distribution. Due to this symmetry, no matter which direction a linear constraint is with respect to the current design point, the shortest distance from the design point to the constraint can be used to calculate the constraint probabilities. The first order reliability method (FORM) and the second order reliability method (SORM) use this characteristic of a normal distribution by first converting a normal distribution $U \sim N(\mu_U, \sigma_U^2)$ into a standard normal distribution $Y \sim N(0, 1^2)$ via

$$Y = \frac{U - \mu_U}{\sigma_U}. \tag{7}$$

After this conversion, FORM states that a constraint probability can be approximated as $\Phi(-\beta)$ where β is the shortest distance from the origin to the constraint function in Y-space. The point that lies on the constraint boundary (also called the limit state function) having the shortest distance to the origin is called the most probable point (MPP), denoted as $\mathbf{x}_j^{\mathrm{M}}$. Each constraint has its own MPP and therefore the number of MPPs is the same as the number of limit state functions (constraints), m. SORM provides a more accurate estimation of constraint probabilities by considering the principal curvatures $\boldsymbol{\kappa}$ of a constraint.

$$\Pr[g_j(\mathbf{X}) > 0] \approx \Phi(-\beta_j) \prod_i (1 + \beta_j \kappa_i)^{-1/2} \tag{8}$$

For independent non-normal random variables, a transformation T is applied to $\mathbf{X}$ such that

$$Y_i = T(X_i). \tag{9}$$

Several such transformations are available in the literature [30], the simplest form given by Eq.(10) requires that the cumulative distribution function (CDF) of the i^{th} random variable X_i at x_i should be the same as the CDF of a standard normal variable at y_i.

$$\Phi(y_i) = F_{X_i}(x_i) \rightarrow y_i = \Phi^{-1}(F_{X_i}(x_i)) \tag{10}$$

Due to the nonlinearity of the transformation, a linear constraint in the X-space will become nonlinear in the Y-space. Applying a first order Taylor series expansion to Eq.(10) around a point x_i^e, one can get the following result.

$$\begin{aligned} y_i &\approx \Phi^{-1}[F_{X_i}(x_i^e)] + \frac{\partial}{\partial x}\{\Phi^{-1}[F_{X_i}(x_i)]\}(x_i - x_i^e) \\ &= \frac{x_i - \{x_i^e - \Phi^{-1}[F_{X_i}(x_i^e)]\phi\{\Phi^{-1}[F_{X_i}(x_i^e)]\}/f_{X_i}(x_i^e)\}}{\phi\{\Phi^{-1}[F_{X_i}(x_i^e)]\}/f_{X_i}(x_i^e)} \end{aligned} \tag{11}$$

If the following assignments are made as the equivalent mean

and equivalent standard deviation of X_i, respectively,

$$\boldsymbol{\mu}_{\mathbf{X}}^e = x_i^e - \Phi^{-1}[F_{X_i}(x_i^e)]\phi\{\Phi^{-1}[F_{X_i}(x_i^e)]\}/f_{X_i}(x_i^e) \quad (12)$$
$$\boldsymbol{\sigma}_{\mathbf{X}}^e = \phi\{\Phi^{-1}[F_{X_i}(x_i^e)]\}/f_{X_i}(x_i^e)$$

then the standard FORM and SORM techniques can be extended to non-normal variables [30, 32].

The typical solution approach for non-normal random variables then involves finding MPPs and equivalent normal parameters. This process may have convergence difficulties and is computationally intensive since calculating the location of the MPP for a nonlinear function is by itself an optimization process. The conversion of constraints from X-space to Y-space via the nonlinear relationship of Eq.(10) is also computationally intensive.

To reduce the number of required calculations in Eq.(3), we start by applying an active set strategy which reduces the number of constraints that must be considered during any iteration of the optimization process. Following the approach detailed in [25], a working set of constraints $\mathcal{G}^k$ is established at each design iteration k which includes constraints that are active or likely active. For constraints inside the working set, we propose here a means to improve the efficiency of calculating Eq.(3) relative to the approach represented by Eqs.(11) and (12).

Before describing this alternative solution approach for non-normal distributions, let us define a reliability contour surface $\Psi = 0$. For standard normal random variables $\mathbf{Y}$, we define a reliability contour surface as a contour satisfying

$$\Psi(\boldsymbol{\mu}_{\mathbf{Y}}, \mathbf{y}) = 0 \; \forall \boldsymbol{\mu}_{\mathbf{Y}} : \{\Pr[l(\boldsymbol{\mu}_{\mathbf{Y}}) > 0] = P_{\mathrm{f}}\} \quad (13)$$

for any linear constraint l. FORM states that the shortest distance from the origin to limit states l must be $\beta = \Phi^{-1}(P_{\mathrm{f}})$. Hence a contour with radius β around the origin is formed. When design variables are not normal, this common radius contour only exists in the standard Y-space. By mapping this common radius contour from Y-space to X-space, a reliability contour surface in the X-space is created.

We propose to use this X-space reliability contour surface $\Psi(\boldsymbol{\mu}_{\mathbf{X}}, \mathbf{x}) = 0$ to identify probabilistic constraint feasibility. A constraint g_j is active if it has a common tangent with the reliability contour surface; it is inactive if $\boldsymbol{\mu}_{\mathbf{X}}$ is feasible and does not intersect with $\Psi = 0$; it is infeasible if $\boldsymbol{\mu}_{\mathbf{X}}$ is infeasible or $\boldsymbol{\mu}_{\mathbf{X}}$ is feasible but it has more than one intersection with $\Psi = 0$. In the following, we will first describe how the $\Psi = 0$ contour can be found directly in the X-space. Then we will describe how to use this reliability contour surface within an active set strategy.

In the Y-space, the reliability contour surface is a β radius contour around the origin as Eq.(14).

$$\sum_{i=1}^{n} y_i^2 = \beta^2. \quad (14)$$

Eq.(10) shows the relationship between Y_i and a non-normal variable X_i. Combining Eq.(10) and (14) we obtain the reliability contour surface in the X-space, Eq.(15).

$$\sum_{i=1}^{n} \left(\Phi^{-1}(F_{X_i}(x_i))\right)^2 = \beta^2 \quad (15)$$

Obtaining Eq.(15) only requires that all CDFs are analytical, which was also necessary using the method of finding equivalent normal distributions. However, the reliability contour method has an advantage since the calculation need be performed only one time, as a pre-processing step, rather than at each design iteration.

As an example consider a constraint $\Pr[g(X_1, X_2) > 0] \leq P_{\mathrm{f}}$ where both design variables have Weibull distributions, their PDF being

$$f_{X_1}(x) = f_{X_2}(x) = \alpha\eta^{\alpha}x^{\alpha-1}e^{-(\frac{x}{\eta})^{\alpha}}$$

where $\eta = 1$, $\alpha = 1.5$. This two dimensional Weibull reliability contour can be written as Eq.(16).

$$\Psi : \left[\Phi^{-1}\left(e^{-(\frac{x_1-\mu_{X_1}}{\eta_1})^{\alpha_1}}\right)\right]^2 + \left[\Phi^{-1}\left(e^{-(\frac{x_2-\mu_{X_2}}{\eta_2})^{\alpha_2}}\right)\right]^2 - \left[-\Phi^{-1}(P_{\mathrm{f}})\right]^2 \quad (16)$$

Figure 4 shows this Weibull reliability contour with $P_{\mathrm{f}} = 1\%$. The accuracy of using the reliability contour surface approach is the same as using FORM. At every design point, the limit state function is transferred from the X-space to the U-space. In FORM, if the U-space limit state function, g_j^U, is tangent to the β-sphere, the tangent point is the MPP and the probability is equivalent to the probability of its linearization at the MPP point. The transformation in Eq.(10) ensures that when the MPP in U-space is mapped back to the X-space it will still be the tangent point between the reliability contour surface and the X-space limit state, g_j. Let the linearization of the limit state at the MPP in X-space be $\hat{g}_j$ and in the U-space be $\hat{g}_j^U$. The probability of violating the constraint in X-space is approximated as the probability of violating $\hat{g}_j$ which translates to $\hat{g}_j^U$ in U-space. Hence, using the reliability contour surface method, we can obtain the same accuracy as FORM. In the optimization routine, the number of required computations is reduced significantly because the reliability contour method is integrated with an active set strategy, such that only constraints in the working set are considered. The point that lies on the reliability contour with the minimal distance to a constraint is called an MPP estimate. The MPP estimate will be the actual MPP for an active constraint, and will be an estimate of the actual MPP for an inactive constraint. Although the MPP estimate and the actual MPP can be significantly different for an inactive constraint, the constraint value at the MPP estimate will always provide correct feasibility information (i.e., "yes" or "no") for the probabilistic constraint it considers.

The relationship between actual MPP values and MPP estimates is illustrated in Figure 5 with two constraints g_1 and g_2. Constraint g_1 is active at the current design point $\boldsymbol{\mu}_{\mathbf{X}}$ while g_2 is inactive. Actual MPPs, denoted as $\mathbf{x}_{\mathrm{MPP}_j}$, are shown as triangles;

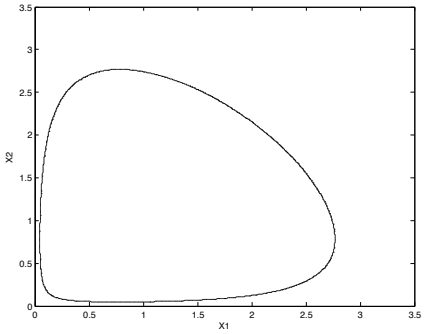

Figure 4. 99% Reliability Contour for Weibull Distributions

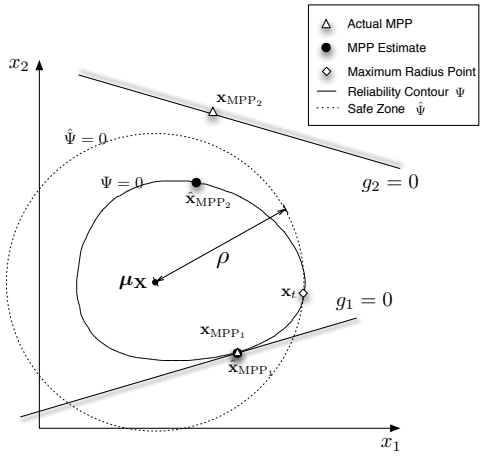

Figure 5. Relationships between MPP values and MPP estimates

MPP estimates, $\hat{\mathbf{x}}_{\mathrm{MPP}_j}$ are shown as circles. The actual MPPs are on the constraint boundary and the MPP estimates are on the reliability contour. Since g_1 is active, $\mathbf{x}_{\mathrm{MPP}_1} = \hat{\mathbf{x}}_{\mathrm{MPP}_1}$.

The location of the MPP estimate on the reliability contour is found by matching the normal vectors (Eq.(17a)) and values (Eq.(17b)) of the reliability contour and constraint boundary.

$$\Psi(\boldsymbol{\mu}_{\mathbf{X}}, \mathbf{x}_{\mathrm{MPP}_j}) = g_j(\mathbf{x}_{\mathrm{MPP}_j}) \tag{17a}$$

$$\frac{\partial}{\partial \mathbf{x}} \Psi(\boldsymbol{\mu}_{\mathbf{X}}, \mathbf{x})\big|_{\mathbf{x}_{\mathrm{MPP}_j}} = \frac{\partial}{\partial \mathbf{x}} g_j(\mathbf{x})\big]\big|_{\mathbf{x}_{\mathrm{MPP}_j}} \tag{17b}$$

To reduce the computational burden in solving Eq.(17a) and (17b), we propose the following. For inactive constraints, the exact locations of MPP estimates are not critical as long as they provide the correct feasibility information. Therefore a "safe zone" of feasibility is created that is computationally less intensive than finding the MPP estimate directly on the reliability contour. This safe zone is created with a common radius emanating from the design point that is constant in all directions and equal to the maximum distance from the design point to the reliability contour (radius = ρ in Fig.5). If the constraint is found to intersect the safe zone reliability contour, then the constraint is included in the active set and the MPP estimate for that constraint is calculated on the actual reliability contour to determine feasibility of the constraint. The radius of safe zone reliability contour is obtained by solving Eq.(18), with the point $\mathbf{x}_t$ serving as the maximal radius point.

$$\begin{aligned} &\max_{\mathbf{x}} \rho = \|\mathbf{x} - \boldsymbol{\mu}_{\mathbf{X}}^k\| \\ &\text{s.t. } \Psi(\boldsymbol{\mu}_{\mathbf{X}}^k, \mathbf{x}) = 0 \end{aligned} \tag{18}$$

The safe zone reliability contour is centered at the current design point and shown in Figure 5.

For highly skewed distributions, the actual reliability contour surface will be very asymmetric and therefore using a constant radius safe zone will be conservative. This conservative estimate may result in additional constraints in the active set, but the net computational burden will still be significantly lower given that considerable gains are made by avoiding unnecessary MPP calculations on the actual reliability surface. Overall, the method has significant speed advantages with equivalent accuracy to existing methods.

The solution approach of using a reliability contour surface and its safe zone reliability contour can be summarized as follows:

Step.1 At the current point $\boldsymbol{\mu}_{\mathbf{X}}^k$, find the gradient of each constraint;
Step.2 Form the reliability contour given all random quantities;
Step.3 Find the safe zone reliability contour radius using Eq.(18);
Step.4 For each constraint, use the constraint gradient to find the MPP estimate on the safe zone reliability contour;
Step.5 For inactive constraints, the safe zone reliability contour is used for calculating MPP estimates;
Step.6 For active constraints, the actual reliability contour surface is used to locate the MPP estimates;
Step.7 Constraint feasibilities are determined via comparison to their values at the MPP estimates.

Consider constraint g_j. The first two steps require calculating ∇g_j and $\Psi(\boldsymbol{\mu}_{\mathbf{X}}^k, \mathbf{x}) = 0$ at $\boldsymbol{\mu}_{\mathbf{X}}^k$. In Step 3 ρ is calculated via Eq.(18) and the safe zone reliability contour is formed as Eq.(19).

$$\hat{\Psi}_{\rho}(\boldsymbol{\mu}_{\mathbf{X}}^k, \mathbf{x}) = \sum_{i=1}^{n} (x_i - \mu_{X_i})^2 - \rho^2 = 0 \tag{19}$$

The MPP estimate $\mathbf{x}_{\mathrm{MPP}_j}$ is calculated as Eq.(20) in Step 4.

$$\hat{\mathbf{x}}_{\mathrm{MPP}_j} = \boldsymbol{\mu}_{\mathbf{X}} + \rho \frac{\nabla g_j}{\|\nabla g_j\|} \tag{20}$$

In Step 5 if $g_j(\hat{\mathbf{x}}_{\mathrm{MPP}_j}) < 0$, g_j is inactive. Otherwise it is active and the actual $\mathbf{x}_{\mathrm{MPP}_j}$ needs to be calculated in Step 6 via Eq.(17a-17b). If $g_j(\mathbf{x}_{\mathrm{MPP}_j}) \leq 0$, the current design point $\boldsymbol{\mu}_{\mathbf{X}}^k$ is feasible to Eq.(1). Otherwise it is infeasible and the feasibility results are sent back to the optimizer.

2.4 Joint Constraint Reliability

Constraints in standard RBDO formulations are written such that the probability of violating each constraint does not exceed an acceptable limit.

$$\Pr[g_i(\mathbf{X}) > 0 \cap g_j(\mathbf{X}) > 0] = \emptyset \; \forall i, j \in \mathcal{K} \tag{21}$$

In an hypothetical RBDO formulation with 100 independent constraints (whose constraint sets are mutually exclusive) and a reliability target of 99% in Eq.(21), the expected number of constraint violations out of the 100 constraints is actually one. Even though so many constraints are unlikely to be independent, the example demonstrates the need for considering joint reliability.

In the airshed problem it is most relevant to consider the probability of ANY constraint being violated, whether that constraint corresponds to a receptor point being considered in Fig.1 or whether multiple pollutants are considered such as CO and NOx. If we consider the probability that any constraint is violated, then we must consider a union of events. Let F_j be the infeasible (failure) domain of constraint g_j. The problem is then written as Eq.(22):

$$\begin{aligned} &\min_{\boldsymbol{\mu}_\mathbf{X}} f(\boldsymbol{\mu}_\mathbf{X}) \\ &\text{s.t. } \Pr\left[\bigcup_{j\in\mathcal{K}} F_j\right] \leq P_f \end{aligned} \tag{22}$$

Calculating the constraint feasibility in Eq.(22) is challenging. In the simplest case with only linear constraints and normally distributed random variables, the probability of union of failure events results in a multivariate normal integral as in Eq.(23) [32].

$$\Phi_m(\mathbf{h}, \mathbf{R}) = \frac{1}{(2\pi)^{m/2}\|\mathbf{R}\|^{1/2}} \int_{-\infty}^{h_m} \cdots \int_{-\infty}^{h_1} e^{-\frac{1}{2}\mathbf{x}^T\mathbf{R}^{-1}\mathbf{x}} dx_1 \cdots dx_m \tag{23}$$

Calculating the exact solutions of Eq.(23) is impractical in most cases. Ditlevsen proposed using an upper and lower bound of Eq.(23) to approximate its true value [33]. He calculates the general upper and lower bounds as

$$\Pr\left[\bigcup_j F_j\right] \leq \sum_{j=1}^{m} \Pr[F_j] - \sum_{j=2}^{m-1} \max_{k<j} \left(\Pr[F_j \cap F_k]\right) \tag{24}$$

$$\Pr\left[\bigcup_j F_j\right] \geq \Pr[F_1] + \sum_{j=2}^{m} \max\left(\Pr[F_j] - \sum_{k=1}^{j-1} \Pr[F_j \cap F_k]\right) \tag{25}$$

The union of multiple failure domains becomes increasingly difficult to calculate with an increasing number of constraints. One advantage of using the upper and lower bounds is that they are calculated from unions of any two failure domains. Once the relationship between two failure surfaces is known, Eq.(24) and (25) are much easier to calculate.

We use a conservative approach by stating that as long as the upper bound in Eq.(24) is less than or equal to an acceptable failure probability P_f, then the overall system has feasible reliability (i.e., it is probabilistically feasible for the joint constraint case). To incorporate this approach within the active set strategy, the upper bound of the joint constraint reliability Eq.(24) is calculated only for constraints in the working set $\mathcal{G}^k$. For constraints that do not have the potential to be violated, it is assumed that their contribution to joint reliability is negligible. The overall process of considering joint constraint reliability in the active set strategy is as follows:

1. Obtain the working set $\mathcal{G}^k$ at the kth iteration from the optimizer;
2. Calculate individual constraint violations for $j \notin \mathcal{G}^k$;
3. Calculate the upper bound of joint constraint reliability for $j \in \mathcal{G}^k$;
4. Return all constraint results to the optimizer.

2.5 Example with non-normal random variables and joint constraint reliability

The importance of considering the joint constraint reliability depends on how much the failure domains of active constraints overlap with each other. For problems with a large portion of overlapping failure domains, considering joint reliability might not make a significant difference. However, for problems without overlapping failure domains of active constraints, joint reliability can change the results quite significantly.

Figure 6 shows a problem with two variables and two linear constraints, Eq.(26), where the random variables X_1 and X_2 have both Weibull distributions with shape and scale parameters being 1.

$$\begin{aligned} &\min_{\mu_{X_1}, \mu_{X_2}} f(\boldsymbol{\mu}_\mathbf{X}) = \mu_{X_1} + \mu_{X_2} \\ &\text{s.t. } \Pr[X_1 > 6] \leq 10\% \\ &\quad \Pr[X_2 > 6] \leq 10\% \end{aligned} \tag{26}$$

If the probability of failure for each constraint is set at 10%, as in Eq.(26), the optimum is computed to be Eq.(26) is $[4.697, 4.697]$. In this case, the probability of violating both constraints is negligible, i.e., $\Pr[g_1 > 0 \cap g_2 > 0] = 0$. The probability of violating either constraint becomes

$$\Pr[g_1 > 0 \cup g_2 > 0] = \Pr[g_1 > 0] + \Pr[g_2 > 0] - \Pr[g_1 > 0 \cap g_2 > 0] \tag{27}$$

and it is actually 20%, making the joint constraint reliability at this design point only 80%. Considering the joint constraint reliability, the problem is reformulated as Eq.(28).

$$\begin{aligned} &\min_{\mu_{X_1}, \mu_{X_2}} f(\boldsymbol{\mu}_\mathbf{X}) = \mu_{X_1} + \mu_{X_2} \\ &\text{s.t. } \Pr[X_1 > 6 \cup X_2 > 6] \leq 10\% \end{aligned} \tag{28}$$

The optimum is now $[4.004, 4.004]$ with a joint reliability being 90%. The failure probability of each constraint in this case is 5%. Figure 6 shows the reliability contours for the two problems. The probability of being in the joint failure domain of both

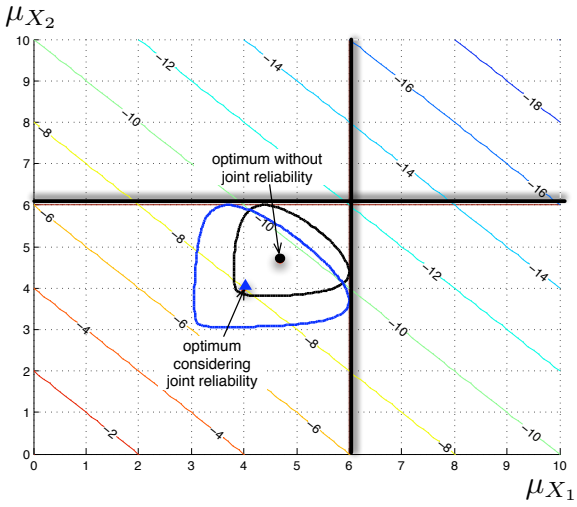

Figure 6. Example of non-normal random variables considering joint constraint reliability

constraints is small. Therefore, to achieve a high joint reliability the reliability contour becomes larger and the design becomes more conservative.

3 Air Pollution Case Study Model Development

In this case study, we are interested in reducing tailpipe emissions from vehicles on the highways to bring the area into compliance with the NAAQS by reducing speed limits. Vehicle operational speed has significant impact on tailpipe emissions [34] and fuel consumption [35]. These relationships are highly nonlinear and subject to inter-vehicle variability as well as operational uncertainties. Setting an appropriate speed limit is inherently a trade-off between driver safety, time savings, vehicle emissions, and fuel economy [36]. In what follows, we first describe the objective function and constraints and then apply the methods developed above. We validate the optimum using Monte Carlo simulation.

3.1 Objective Function

Several studies have focused on the effects of regulatory speed limits on safety and other economic metrics (e.g., see [37]). Eq.(29) describes an objective that considers safety and time savings as a function of speed limit [38].

$$f(v) = 1000 \times D(v) + c(v) \tag{29}$$

where

$$D(v) = 2.11 \times 10^{-6} v^4 - 5.03 \times 10^{-4} v^3 + 0.0454 v^2 - 1.838 v + 32.2189 \tag{30}$$

Here $D(v)$ is a measure of safety in terms of property damage (in thousand dollars) per 100 million vehicle-miles and is defined as the probability of being involved in a crash multiplied by the severity of each crash at different speeds. Solomon [7, 39] found that the probability of being involved in a crash per vehicle-mile as a function of on-road vehicle speeds follows a U-shaped curve. Speed values around the median speed have the lowest probability of being in a crash. Crash severity is measured by speed differences before and after the crash [40]. Assuming the final speed after the crash is zero, this crash severity measure is proportional to the speed before the crash. Fitting the data from [7], we obtain the safety measure given in Eq.(30) as the overall price society is willing to pay for each accident.

The measure $c(v)$ reflects the value of time savings associated with increased vehicle velocity. Assuming the average wage is w (dollars per hour), $c(v)$ is used as the cost of an hour spent travelling without working. The overall travelling time for a trip of length s (in kilometers) is

$$t = s/v \tag{31}$$

where v(km/hr) is the speed of an on-road vehicle. The overall cost (dollars) for trip s is then

$$c = w \times t. \tag{32}$$

Combining the societal costs of property damage (medical and social welfare) and cost of time spent on travelling, the objective function represents an economic measure of the pros and cons of driving at a specific speed.

3.2 Constraint Functions

The constraints are that the overall emissions of carbon monoxide (CO) and nitrogen oxides (NOx) from on-road vehicle tailpipe emissions cannot lead to a local violation of the values set by the National Ambient Air Quality Standards (NAAQS). Here we will consider only the one-hour standard. The current NAAQS states that the one-hour concentration of CO cannot exceed 40 mg/m^3 and the annual average concentration of NOx cannot exceed 100 μg per cubic meter. The NAAQS does not state one-hour limit of NOx, and therefore in this example the one-hour ambient air quality standard for NOx (470 μg/m^3) in California is implemented. For the building block problem of Fig.1, we use the infinite line source dispersion model Eq.(33) as described by [13] while recognizing that this simplistic infinite line source can be readily replaced with more complex modelling approaches such as found in CALINE4 [23].

$$g_j(x) = \sum_{i=1}^{2} \frac{2q_i}{\sqrt{2\pi}\sigma_{z_i} U_{h_i}} \tag{33}$$

In Eq.(33) the index i represents highway systems, j represents different pollutants, q is the emission rate, which is the product of emission factor (EF) of the vehicles and the vehicle traffic

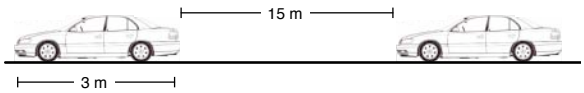

Figure 7. Traffic Modeling

density T in Eq.(34):

$$q(\text{gram/second}) = EF(\text{gram/vehicle}) \times T(\text{vehicle/second}) \tag{34}$$

We assume that the vehicles on both highway systems are mid-size gasoline-powered passenger vehicles that are identical to each. The Advanced Vehicle Simulator (ADVISOR) [41] is used to obtain emission factors for the vehicle at different speeds. In the highway driving cycle cruise speed is set at the maximum speed limit, and so a relationship between speed and emissions factors for CO and NOx is found as in Eq.(35) and (36) with the sum of the squares of the deviations (R^2) being 0.9943 and 0.8935 respectively.

$$\begin{aligned} EF_{\text{CO}}(v) = &-7.01\times10^{-9}v^5 + 2.86\times10^{-6}v^4 - 4.48\times10^{-4}v^3 \\ &+ 3.39\times10^{-2}v^2 - 1.256v + 20.88 \end{aligned} \tag{35}$$

$$\begin{aligned} EF_{\text{NOx}}(v) = &2.00\times10^{-10}v^5 - 5.36\times10^{-8}v^4 + 5.13\times10^{-6}v^3 \\ &- 1.80\times10^{-4}v^2 - 4.10\times10^{-4}v + 0.48 \end{aligned} \tag{36}$$

Although emission rates may differ between vehicles due to operational variation and maintenance, these uncertainties were not considered in this example. Highway traffic is modelled as constant flow per second with each highway having four lanes in each direction. The constant-flow traffic is shown Fig.7 and modeled as Eq.(37).

$$T(v) = v(\text{meter/second}) \div (3+15)(\text{meter/vehicle}) \tag{37}$$

3.3 Quantification of Uncertainties

Uncertainty in Eq.(33) comes from four sources : wind speed and direction, dispersion coefficient and driver speed responses to posted speed limits.

Wind Speed and Direction

The probability density functions of wind speed and wind directions are modelled based on McWilliams et al. [10,42]. Unlike the method of Ramirez which uses a two-parameter Weibull distribution [43], McWilliams et al. decompose wind speed into two components: one along the prevailing wind direction and one perpendicular to it. We assign the actual wind speed as U_h, the prevailing wind direction as ψ, the wind speed along the prevailing wind direction as U_y, and the speed perpendicular to the prevailing wind direction as U_x. Figure 8 illustrates the relationship between the wind components. McWilliams et al. [10] used

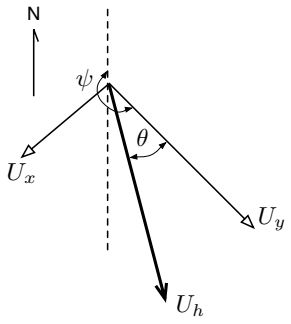

Figure 8. Ambient Wind Direction

the model with the wind speed distributions U_y and U_x being normally distributed as Eq.(38).

$$U_y \sim N(\mu,\sigma),\;\; U_x \sim N(0,\sigma) \tag{38}$$

According to McWilliams [42], the distributions for the observed wind speed U_h and wind direction θ can then be calculated since $U_h = \sqrt{U_x^2 + U_y^2}$ and $\theta = \tan(U_y/U_x)$. Eq.(39) is the resulting PDF for U_h and θ, where I_0 is the modified Bessel function of the first kind.

$$f_{U_h}(v) = \left[\frac{1}{\sigma^2} v e^{-\frac{v^2}{2\sigma^2}}\right] \cdot e^{-\frac{\mu^2}{2\sigma^2}} \cdot I_0\left(\frac{\mu}{\sigma^2}v\right) \tag{39}$$

$$f_\theta(\theta) = \frac{1}{2\pi} e^{-\frac{\mu^2}{2\sigma^2}} \left[1 + \frac{\mu}{\sigma}\sqrt{2\pi}\sin(\theta)\cdot\Phi\left(-\frac{\mu}{\sigma}\sin(\theta)\right)\cdot e^{\frac{1}{2}\left(\frac{\mu}{\sigma}\sin(\theta)\right)^2}\right]$$

Using the method described in [42], the data obtained from the National Climatic Data Center (NCDC) [12] indicates that the prevailing wind direction during the summer in Detroit, Michigan, during rush hour (5pm to 6pm) is at 215 degrees with $\mu = -0.825$ and $\sigma = 3.177$ in Eq.(39). Rush hour is selected as it is expected for the situation in Fig.1 that this is the time period when the constraints are most likely to be violated. Figures 9a and 9b indicate acceptable agreements between data histograms and the PDF predictions using Eq.(39).

Dispersion Coefficient

In a Gaussian dispersion model, the dispersion coefficients σ_z for both roads are a function of the distance from the site to the line source L. The dispersion coefficient σ_z is typically represented by three parameters c,d,f [44].

$$\sigma_z = cL^d + f \tag{40}$$

Values of c,d,f depend on an ambient atmospheric condition called 'stability class'. Stability class describes the effective vertical mixing of a parcel of air existing in the airshed and is commonly determined as shown in Table 1. Table 2 shows the values of c,d,f for different stability classes [13]. Solar insolation from NCDC data is quantified as cloudiness or sky cover, which is

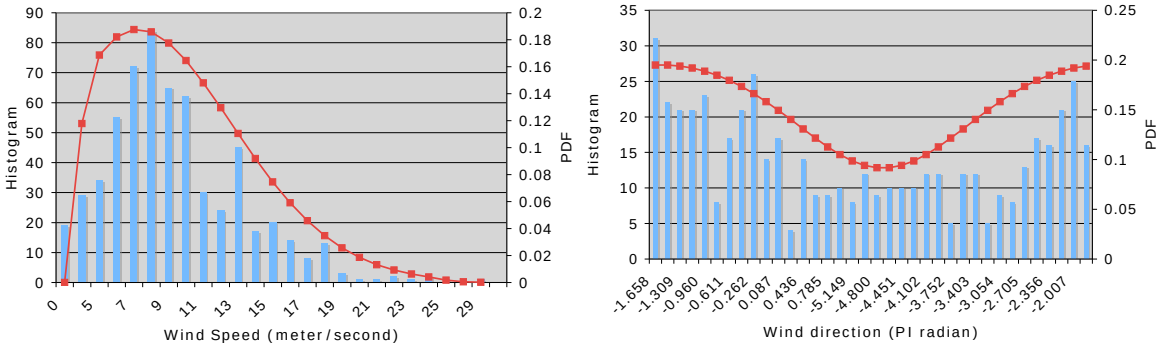

(a) Wind Speed (b) Wind Direction

Figure 9. Histogram and PDF prediction

measured from $0/8$ to $8/8$ with $0/8$ being clear sky and $8/8$ being overcast. $0/8$ to $3/8$ is considered as strong insolation, $3/8$ to $6/8$ is considered as moderate insolation, and above $6/8$ is considered considered as slight insolation. The data for the Detroit area reveal that solar insolation in summer says is independent of wind speed and adequately modelled as a uniform distribution.

Table 1. Atmospheric Stability Classifications [13]

Surface Wind Speed (m/s)	Day solar insolation			Night cloudiness	
	Strong	Moderate	Slight	Cloudy	Clear
< 2	A	A-B	B	E	F
$2-3$	A-B	B	C	E	F
$3-5$	B	B-C	C	D	E
$5-6$	C	C-D	D	D	D
> 6	C	D	D	D	D

Given distributions of solar insolation and wind speed, distributions of c, d, f can be obtained from Table 1 and they are discrete. The existence of discrete variables in the Gaussian dispersion model means that a probabilistic constraint will be formulated as Bayesian conditional probability such that continuous distributions are used to approximate the distributions of c, d, f as discussed in Section 2.2. The dispersion coefficient σ_z is calculated as shown in Eq.(41).

$$f_{\sigma_z} \approx \sum_{i=1}^{7} \phi(\mu_{z_i}, .1^2) \times p_i\% \tag{41}$$

where $\boldsymbol{\mu_z} = [15.96, 25.87, 32.44, 42.69, 51.37, 100.08, 124.07]$, $\mathbf{p} = [18.00, 4.64, 27.19, 13.05, 21.83, 10.93, 4.36]$.

The dispersion coefficient can be modeled as continuous blending functions rather than discrete. Turner's model [45] as shown in Table 2 is used in the context of this paper due to the absence of such a blending function. In addition, Turner defined Table 1 based on the cloudiness in summer or based on the angle of the sun above the horizon. The example is focused on summer days, therefore the need to calculate the sun angle is suppressed.

Table 2. Values of the constants a, c, d and f in Eq.(40) [13]

		$L \leq 1$ km			$L \geq 1$ km		
Stability	a	c	d	f	c	d	f
A	213	440.8	1.941	9.27	459.7	2.094	-9.6
B	156	106.6	1.149	3.3	108.2	1.098	2.0
C	104	61.0	0.911	0	61.0	0.911	0
D	68	33.2	0.725	-1.7	44.5	0.516	-13.0
E	50.5	22.8	0.678	-1.3	55.4	0.305	-34.0
F	34	14.35	0.740	-0.35	62.6	0.180	-48.6

Vehicle Speed

A Federal Highway Administration report [46] indicates that for highways with speed limit 55 MPH, an average speed of 56.9 MPH and 85th percentile speed 64.0 are observed. Based on this study, we assume that vehicle speed is normally distributed with mean equaling to the speed limit and a standard deviation $\sigma_V = 7$ MPH.

4 Results and Discussion

Solving the problem deterministically, the results show that none of the air quality constraints are active and the optimum is $v^* = 70.26$ MPH (31.41 m/s). At this speed limit, pollution concentration during rush hour at the receptor location of Fig.1

are 0.9 mg/m^3 for CO and 200 μg/m^3 for NOx. Interestingly, however, after random design variables/parameters are considered, this deterministic optimum is more than 99% reliable with respect to the CO standard but only 80% reliable with respect to the NOx standard. Without changing the speed limit, the NOx standard would need to be set at 1410μg per cubic meter to satisfy a 90% reliability level. The example demonstrates that when significant variability in system parameters exists, constraint violations can occur even when constraints are not active deterministically. Therefore, without incorporating uncertainty into design optimization, the compliance of NAAQS using deterministic optimization is not sufficiently reliable.

Letting the desired compliance reliability be 90% without considering joint reliability, results in an optimum speed limit reduced to 54.56 MPH (24.34 m/s). The overall societal cost increases from \$597,910 to \$792,040, an approximately 32.47% increase. The example demonstrates that extensions of the active set reliability contour approach to probabilistic problems can be made to realistic policy optimizations without a large concern regarding computational burden.

By considering joint constraint reliability at 90%, the optimal speed limit is further reduced to 53.79 MPH (24.05 m/s). Table 3 compares the results with and without considering joint constraint reliability. The previous probabilistic optimum using Eq.(1) has reliability to comply to current NAAQS of NOx and CO as 89.70% and 99.23% respectively. The actual joint reliability at this speed limit is 89.10%. The probabilistic optimum considering joint constraint reliability in the optimization formulation (Eq.(2)) has the desired joint reliability (90.02%).

The change of reliability contour surfaces with and without considering joint reliability constraint is shown in Fig.10 with results from Table 4. Figure 10 illustrates the design space with respect to vehicle speed and wind speed. The constraint boundaries with different NOx regulations (470 and 1410 μg/m^3) and a single CO regulation (40 mg/m^3) are plotted. From the figure, it is seen that with the original regulation, the reliability contour surface must move to 53.79MPH (24.04 m/s). The NOx constraint (470 μg/m^3) dominates the CO constraint, and therefore the differences with and without considering joint constraint reliability in Table 3 is relatively small. To demonstrate more clearly the difference a joint reliability calculation can make, we assume that the one-hour NOx constraint was actually set at 1470 μg/m^3. Results in Table 4 show that in this case, without considering joint reliability, there is a 88.2 % reliability of violating any constraints. The enlarged reliability contour indicates the 1.9 % joint reliability difference from Table 4. In this case, the joint reliability needs to be considered because points that do not violate NOx might violate CO.

The complexity of the CDFs and PDFs of the uncertainties makes sampling methods impractical. Typically, random samples are created by generating N random samples ξ_i from $[0,1]$ uniformly. Inverse CDFs are then used to find the corresponding

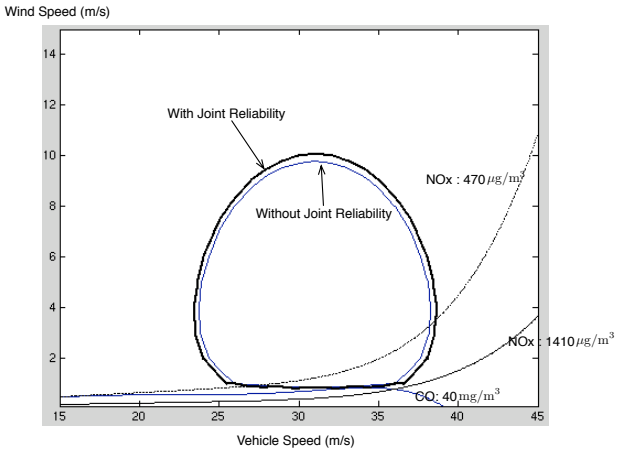

Figure 10. Reliability contour surfaces before and after considering joint constraint reliability

random sample via Eq.(42).

$$x_i = F_{X_i}^{-1}(\xi_i) \tag{42}$$

Obtaining the inverse of CDF is computationally intensive and a large number of random samples need to be generated to maintain high accuracy. Our experience in this example shows that the computational requirement for generating random samples prohibit many sampling techniques from being plausible.

Overall, the method is straightforward. One issue to consider is that calculating the maximum radius in Eq.(18) appears to be dependent on the algorithm used. For a gradient-based algorithm, a good starting point must be selected such that the problem can converge while satisfying the equality constraint. On the other hand, non-gradient algorithms have difficulties satisfying the equality. Here we suggest that a combination of both algorithms be used. A non-gradient based algorithm is first applied and the optimum is selected as the starting point for the gradient based algorithm. Although it is a process requiring significant effort, Eq.(18) needs only to be executed once for the entire problem. This modest amount of pre-processing opens the door to rapid calculation of design optima for large scale problems with non-normal variables/parameters and joint reliability.

In addition, to implement the proposed method for discrete random variables, the converted continuous distributions might have some impacts numerically in practice. The selection of the standard deviation for each Gaussian distribution in Eq.(6) will affect the approximation accuracy directly. Appropriate standard deviation values need to be determined by conducting sensitivity analysis. The highly asymmetric approximated distribution will increase the computation complexity to find the reliability contour and safe zone.

The results of this case study depend highly on the assumptions made in the model, but they should motivate future stud-

Table 3. Probabilistic Results with and without Considering Joint Reliability

	consider individual reliability	consider joint reliability
optimal speed limit	54.56 MPH (24.34 m/s)	53.79 MPH (24.05 m/s)
NOx compliance reliability†	89.7%	90.0%
CO compliance reliability†	99.2%	99.5%
Joint constraint reliability†	89.1%	90.0%

†: using Monte Carlo Simulation with 1 million samples

Table 4. Probabilistic results with and without considering joint reliability for the new NOx standard (1410 μg/m^3)

	consider individual reliability	consider joint reliability
optimal speed limit	70.26 MPH (31.41 m/s)	69.53 MPH (31.09 m/s)
NOx compliance reliability†	89.4%	92.1%
CO compliance reliability†	90.7%	91.9%
Joint constraint reliability†	88.2%	90.1%

†: using Monte Carlo Simulation with 1 million samples

ies using more complex constitutive models. In this case study, we assumed that highway traffic is modeled as the constant flow shown in Fig.7 and both highway systems have identical traffic characteristics; vehicles on the highways are identical and they are modeled via ADVISOR as compact vehicles ; driving cycles of highway vehicles follow the ADVISOR highway driving cycle with the speed limited to the allowable maximum speed; solar insolation is independent with wind speed; distributions of observed vehicle speeds follow a normal distribution with the standard deviation being constant; weather data from NCDC can represent 5-6pm, the peak hours, in summer adequately; highway vehicles are the exclusive source of pollution acting on the area; all other uncertainties are assumed negligible.

5 ACKNOWLEDGMENTS

This research was partially supported by the Automotive Research Center, a U.S. Army Center of Excellence in Modeling and Simulation of Ground Vehicles at the University of Michigan. This support is gratefully acknowledged.

REFERENCES

[1] National Highway Traffic Safety Administration. Automobile fuel economy. Technical Report Title 49 U.S. Code, Chapter 329, U.S. Department of Transportation, November 2000.

[2] Internal Revenue Service. Publication 510 - gas guzzler tax, 2005. Department of Treasury.

[3] Office of Mobile Sources. Emission facts - the history of reducing tailpipe emissions. Technical Report EPA420-F-99-017, Environmental Protection Agency, U.S., May 1999.

[4] Office of Mobile Sources. Minor amendments to inspection/maintenance program evaluation requirements. Technical Report EPA420-F-97-052, Environmental Protection Agency, U.S., August 1997.

[5] A. Mekky. Toll revenue and traffic study of highway 407 in toronto. *Transportation Research Record*, 1498:5–15, 1995.

[6] M.B. Yildirim and D.W. Hearn. A first best toll pricing framework for variable demand traffic assignment problems. *Transportation Research Part B: Methodological*, 39(8):659–678, 2005.

[7] D. Solomon. Accidents on main rural highways related to speed, driver, and vehicle. Technical report, U.S. Department of Commerce/Bureau of Public Roads, 1964.

[8] J.N. Siddall. *Probabilistic Engineering Design - Principles and Applications*. Marcel Dekker, New York, 1983.

[9] J. Tu, K.K. Choi, and Y.H. Park. New study on reliability-based design optimization. *Journal of Mechanical Design*, 121(4):557–564, 1999.

[10] B. McWilliams, M.M. Newmann, and D. Sprevak. Probability distribution of wind velocity and direction. *Wind Engineering*, 3(4):269–273, 1979.

[11] Y. Zhang, G.A. Bishop, and D.H. Stedman. Automobile emissions are statistically andgamma;-distributed. *Environmental Science and Technology*, 28(7):1370–1374, 1994.

[12] National Climate Data Center.

http://www.ncdc.noaa.gov/oa/ncdc.html. U.S. Department of Commerce.

[13] M.M. Gilbert. *Introduction to Environmental Engineering and Science*. Prentice Hall, New Jersey, second edition, 1996.

[14] J. Fine, L. Vuilleumier, S. Reynolds, P. Roth, and N. Brown. Evaluating uncertainties in regional photochemical air quality modeling. *Annual Review of Environment and Resources*, 28:59–106, 2003.

[15] H. Huang, Y. Akutsu, M. Arai, and M. Tamura. Two-dimensional air quality model in an urban street canyon: Evaluation and sensitivity analysis. *Atmospheric Environment*, 34(5):689–698, 2000.

[16] S. Vardoulakis, B.E.A. Fisher, N. Gonzalez-Flesca, and K. Pericleous. Model sensitivity and uncertainty analysis using roadside air quality measurements. *Atmospheric Environment*, 36(13):2121–2134, 2002.

[17] R.D. Stephens. Remote sensing data and a potential model of vehicle exhaust emissions. *Journal of the Air and Waste Management Association*, 44(11):1284–1292, 1994.

[18] M. Andre and U. Hammarstrom. Driving speeds in europe for pollutant emissions estimation. *Transportation Research, Part D: Transport and Environment*, 5(5):321–335, 2000.

[19] H.C. Frey and J. Zheng. Quantification of variability and uncertainty in air pollutant emission inventories: Method and case study for utility nox emissions. *Journal of the Air and Waste Management Association*, 52(9):1083–1095, 2002.

[20] D.L. Freeman, R.T. Egami, N.F. Robinson, and J.G. Watson. Methodology for propagating measurement uncertainties through dispersion models. In *Proceedings 76th Air Pollution Control Association Annual Meeting*, volume 2, page 15, 1983.

[21] M.S. Bergin and J.B. Milford. Application of bayesian monte carlo analysis to a lagrangian photochemical air quality model. *Atmospheric Environment*, 34(5):781–792, 2000.

[22] A. Yegnan, D.G. Williamson, and A.J. Graettinger. Uncertainty analysis in air dispersion modeling. *Environmental Modelling and Software*, 17(7):639–649, 2002.

[23] P. Benson. CALINE4 - a dispersion model for predicting air quality concentrations near roadways. Technical Report FHWA/CA/TL-84/15, California Department of Transportation, November 1984.

[24] K.-Y. Chan, S. J. Skerlos, and P.Y. Papalambros. An adaptive sequential linear programming algorithm for optimal design problems with probabilistic constraints. *Journal of Mechanical Design (to appear)*, 2006.

[25] K.-Y. Chan, S.J. Skerlos, and P.Y. Papalambros. Monotonicity and active set strategies in probabilistic design optimization. *Journal of Mechanical Design - Special issue on "Risk-Based and Robust Design" (to appear)*, 2006.

[26] W.F. Dabberdt and E. Miller. Uncertainty, ensembles and air quality dispersion modeling: Applications and challenges. *Atmospheric Environment*, 34(27):4667–4673, 2000.

[27] L. Liu, G.H. Huang, Y. Liu, G.A. Fuller, and G.M. Zeng. A fuzzy-stochastic robust programming model for regional air quality management under uncertainty. *Engineering Optimization*, 35(2):177–199, 2003.

[28] O. Ditlevsen. Principle of normal tail approximation. *ASCE J Eng Mech Div*, 107(6):1191–1208, 1981.

[29] M. Hohenbichler and R. Rackwitz. Non-normal dependent vectors in structural safety. *ASCE J Eng Mech Div*, 107(6):1227–1238, 1981.

[30] R.E. Melchers. *Structural Reliability - Analysis and Prediction*. Ellis Horwood Limited, Chichester, England, 1987.

[31] R. Rackwitz. Reliability analysis-a review and some perspective. *Structural Safety*, 23(4):365–395, 2001.

[32] M. Hohenbichler and R. Rackwitz. First-order concepts in system reliability. *Structural Safety*, 1(3):177–188, 1983.

[33] O. Ditlevsen. Narrow reliability bounds for structural systems. *Journal of Structural Mechanics*, 7(4):453–472, 1979.

[34] R. Joumard. Influence of speed limits on road and motorway on pollutant emissions. *Science of the Total Environment*, 59:87–96, 1986.

[35] J.R. Kenworthy, H. Rainford, P.W. G. Newman, and T.J. Lyons. Fuel consumption, time saving and freeway speed limits. *Traffic Engineering and Control*, 27(9):455–459, 1986.

[36] K.C. Sinha. To increase or not to increase speed limit: a review of safety and other issues. In *Proceedings of the Conference on Traffic and Transportation Studies*, pages 1–8, Jul 31 - Aug 2 2000.

[37] Transportation Research Board (TRB). *Managing Speed, Review of Current Practice for Setting and Enforcing Speed Limits*. National Research Council, Washington, DC, 1998. Special Report 254.

[38] O. Ashenfelter and M. Greenstone. Using mandated speed limits to measure the value of a statistical life. *Journal of Political Economy*, 112(1):2, 2004.

[39] E. Hauer. Accidents, overtaking and speed control. *Accident analysis and prevention*, 3(1):1–13, 1971.

[40] H. Joksch. Velocity change and fatality risk in a crash - a rule of thumb. *Accident Analysis and Prevention*, 25(1):103–104, 1993.

[41] T. Markel, A. Brooker, T. Hendricks, V. Johnson, K. Kelly, B. Kramer, M. O'Keefe, S. Sprik, and K. Wipke. Advisor: A systems analysis tool for advanced vehicle modeling. *Journal of Power Sources*, 110(2):255–266, 2002.

[42] B. McWilliams and D. Sprevak. Estimation of the parameters of the distribution of wind speed and direction. *Wind*

Engineering, 4(4):227–238, 1980.

[43] P. Ramirez and J.A. Carta. Influence of the data sampling interval in the estimation of the parameters of the weibull wind speed probability density distribution: A case study. *Energy Conversion and Management*, 46(15-16):2419–2438, 2005.

[44] D.O. Martin. The change of concentration standard deviation with distance. *Journal of the Air Pollution Control Association*, 26, 1976.

[45] D.B. Turner. *Workbook of Atmospheric Dispersion Estimates*. U.S. Environmental Protection Agency, Washington, DC, 1970.

[46] FHWA. Travel speeds, enforcement efforts , and speed-related highway statistics. Technical Report FHWA-SA-95-051, U.S. Department of Transportation, October 1995.